A Correction Algorithm for Rotor-Induced Airflow and Flight Attitude Changes during Three-Dimensional Wind Speed Measurements Made from A Rotary Unmanned Aerial Vehicle

Yanrong Yang[1+], Yuheng Zhang[1+], Tianran Han[1], Conghui Xie[2], Yayong Liu[2], Yufei Huang[1], Jietao Zhou[1], Haijiong Sun[1], Delong Zhao[3], Kui Zhang[4], Shao-Meng Li[1*]

[1]College of Environmental Sciences and Engineering, Peking University, Beijing 100871, China

[2]Laboratory of Gas Instrument Testing, Center for Environmental Metrology, National Institute of Metrology, Beijing 100029, China

[3]Beijing Weather Modification Center, Beijing 100089, China

[4]Beijing Wisdominc Technology Co., Ltd, Beijing 100070, China

+Contributed equally to the work

Correspondence to: Shao-Meng Li (shaomeng.li@pku.edu.cn)

Abstract. A hexacopter unmanned aerial vehicle (UAV) was fitted with a three-dimensional sonic anemometer to measure three-dimensional wind speed. To obtain accurate results for three-dimensional wind speeds, we developed an algorithm to correct biases caused by the rotor-induced airflow disturbance, UVA movement, and attitude changes in the three-dimensional wind measurements. The wind measurement platform was built based on a custom-designed integration kit that couples seamlessly to the UAV, equipped with a payload and the sonic anemometer. Based on an accurate digital model of the integrated UAV-payload-anemometer platform, computational fluid dynamics (CFD) simulations were performed to quantify the wind speed disturbances caused by the rotation of the UAV's rotor on the anemometer during the UAV's steady flight under headwind, tailwind, and crosswind conditions. Through analysis of the simulated data, regression equations were developed to predict the wind speed disturbance, and the correction algorithm for rotor disturbances, motions, and attitude changes was developed. To validate the correction algorithm, we conducted a comparison study in which the integrated UAV flew around a meteorological tower on which three-dimensional wind measurements were made at multiple altitudes. The comparison between the corrected UAV wind data and those from the meteorological tower demonstrated an excellent agreement. The corrections result in significant reductions in wind speed bias caused mostly by the rotors, along with notable changes in the dominant wind direction and wind speed in the original data. The algorithm enables reliable and accurate wind

speed measurements in the atmospheric boundary layer made from rotorcraft UAVs.

Keywords: UAV; Rotor Disturbance; Three-dimensional Wind; Correction Algorithm

1 Introduction

Wind measurement is crucial in various fields of research and application, including meteorology and environmental sciences. Accurate wind characteristics facilitate modeling of atmospheric transport patterns (Gryning et al., 1987; Stockie, 2011), remote sensing data verification (Drob et al., 2015), model input data assimilation (Gousseau et al., 2011; Vardoulakis et al., 2003) and digital modeling result optimization (Booij et al., 1999; Van Hooff and Blocken, 2010). In particular, wind profile measurements near surface can improve the understanding of atmospheric boundary layer (ABL) dynamics and micrometeorological turbulence at the surface (Seibert et al., 2000), allowing detailed understandings and model description of energy and mass exchanges between air and surfaces and transport processes.

The recent development of unmanned aerial vehicles (UAVs) has provided an opportunity for the measurement of wind fields in three dimensions with high spatial resolutions (Mcgonigle et al., 2008; Martin et al., 2011; Kim and Kwon, 2019). The small size, low flight altitude, high mobility and ability to assemble sensing devices make UAVs ideal platforms from which to measure wind in the ABL (Thielicke et al., 2021; Shaw et al., 2021; Stewart et al., 2021). Multirotor UAVs allow flexible control of flight attitude and stationary hovering, and can carry varying payloads depending on the number of rotors (Villa et al., 2016; Riddell, 2014; Bonin et al., 2013; Stewart et al., 2021), offering significant advantages in capturing high-resolution wind characteristics in low-altitude conditions (Anderson and Gaston, 2013; Mcgonigle et al., 2008).

UAVs are often employed to measure wind characteristics both directly and indirectly. Indirect measurement methods involve utilizing pre-installed sensors on the UAV (Elston et al., 2015), in conjunction with specialized flight patterns and wind retrieval algorithm (Bonin et al., 2013; Rautenberg et al., 2018; Gonzalez-Rocha et al., 2019) to achieve wind speed measurement. ~~Although this method is straightforward to operate, it does not accurately reflect actual wind conditions during flight.~~ While these methods offer advantages of operational simplicity and cost-effectiveness, their core principle relies on inversely estimating wind speed through dynamic parameters such as thrust, attitude angles, and flight velocity (Crowe et al., 2020; Donnell et al., 2018; Sikkel et al., 2016; Simma et al., 2020). However,

their accuracy is critically dependent on both the measurement precision of inertial measurement unit (IMU) and the computational reliability of inversion algorithms. Specifically, inherent noise interference in IMU sensors (e.g., gyroscope's angular rates can be severely affected by external disturbances up to 0.5 °/s) (Hoang et al., 2021; Neumann and Bartholmai, 2015), combined with uncertainties in parameter configuration within inversion algorithms (the root mean squared errors (RMSE) of wind speed estimation is 1-1.4) (Bonin et al., 2013), can lead to significant deviations in wind speed estimations. Furthermore, these methods typically assume constant aerodynamic parameters for UAVs, an assumption that often fails to hold in practical complex wind field environments (Bonin et al., 2013).

In contrast, Ddirect measurement methods entail installing additional wind sensors on the UAV to obtain real-time wind information in the field. Porous probes (Soddell et al., 2004; Spiess et al., 2007), pitot tubes (Niedzielski et al., 2017; Langelaan et al., 2011), and anemometers (Rogers and Finn, 2013; Nolan et al., 2018) are commonly used sensors. Sonic anemometers are a more prevalent choice for rotorcraft UAVs, capable of measuring wind speed by detecting changes in the speed of sound travel between different sensors (Thielicke et al., 2021). Recent experiments have demonstrated that under highly turbulent conditions, UAV equipped with properly installed sonic anemometers in wind tunnels can achieve wind speed measurements with RMSE ranging from 4.3% to 15.5% compared to bistatic lidar (Thielicke et al., 2020). Due to the increasing use of rotorcraft UAVs for wind measurements, sonic anemometers are recognized as one of the most promising methods in terms of measurement accuracy and precision.

Sonic anemometers have been mounted onto rotary-wing UAVs for measuring wind speed to varying degrees of success. Typically, an anemometer is mounted at a position along the central axis above the UAV, with data adjusted for the additional wind speed signals induced by UAV motion and attitude changes. Nevertheless, the strong airflow perturbations caused by the rotating propellers can distort real wind flow patterns and significantly affect the accuracy of wind measurements (De Divitiis, 2003). However, these distortions were not considered in the adjustment algorithms. To address this issue, researchers have developed several new correction methods. The first method involves mounting the anemometer along the central axis high above the UAV where the rotor wash effects are believed to be limited on the wind speed measurement (Shimura et al., 2018; Barbieri et al., 2019). Johansen concluded that anemometers at about 40 to 45 mm above the multi-rotor plane of small UAV the flow

88   influences from rotors are negligible (Johansen et al., 2015). However, it may not be suitable for

89   hexacopters and octocopters due to the high position required, which may raise safety and flight control

90   concerns. The second method involves new corrections based on experiments in an indoor area to

91   measure wind velocity signal bias caused by the rotors during flight and then subtracting the bias

92   (Palomaki et al., 2017). Palomaki et al. (2017) quantified rotor-induced wind speed errors as 0.5 m/s

93   compared to tower-mounted anemometers and subtracted these errors from the directly measured wind

94   speed values in subsequent analyses (Palomaki et al., 2017). However, this method is limited by the size

95   of the indoor area, inadequate for full simulations of real UAV rotor speed and attitude changes during

96   flight, and insufficient for the development of a comprehensive correction scheme. Additionally, it does

97   not take into account the detailed coupling of true winds with propeller downwash. The third method is

98   similar to the second except the use of wind tunnels to establish a more accurate relationship between

99   increased air speed and UAV motion or attitude parameters (Thielicke et al., 2021; Neumann and

100 Bartholmai, 2015). While effective in determining numerical relationships, the method is limited by the

101 high cost of wind tunnel experiments (Dao et al., 2023), and more importantly, by the additional errors

102 introduced by reflected airflows from the wind tunnel walls and ground (Haleem, 2021; Pettersson and

103 Rizzi, 2008), as well as the same issues of full simulations of real UAV rotor speed and attitude changes

104 during flight.

105   The flaws in these correction methods could be addressed by using computational fluid dynamics

106 (CFD) simulations to analyze the airflow generated by the UAV's propellers. As far as we know, CFD

107 has been employed to analyze airflow patterns around drones but hasn't been utilized to correct wind

108 measurements obtained from UAVs (Oktay and Eraslan, 2020; Hedworth et al., 2022). In this paper, we

109 introduce a three-dimensional wind speed correction algorithm for sonic anemometer wind

110 measurements taken from a rotary UAV. This algorithm considers the rotor-induced airflow of the UAV,

111 based on CFD simulations, along with the UAV's motion and attitude changes during flight. The

112 accuracy of the algorithm is confirmed by comparing the corrected wind speeds with those measured

113 from a meteorological tower at multiple altitudes. These results could contribute to ongoing efforts

114 aimed at enhancing the performance and reliability of UAV-based wind speed measurement techniques.

115 Additionally, they pave the way for potential applications, such as quantifying pollutant emissions from

116 industrial complexes (Han et al., 2023).

2 Method

2.1 ~~Equipment and~~ Digital Model Representation and Simulation Tool

2.1.1 Digital Model Representation

A six-rotor UAV (KWT-X6L-15, ALLTECH, China), equipped with six 32 cm diameter propellers driven by M10 KV100 brushless DC motors, was the platform from which wind was measured. The UAV has a symmetrical motor wheelbase of 1765 mm with an unloaded takeoff weight of 22.5 kg and a maximum flight speed of 18 m s^{-1}. It has a flight endurance > 30 min while carrying its maximum payload of 15 kg.

A miniature three-dimensional ultrasonic anemometer (Trisonica-Mini Wind and Weather Sensor, Anemoment, America) allowed the measurement of wind speed under 15 m s^{-1} with an accuracy of $\pm$ 0.1 m s^{-1} and a resolution of 0.1 m s^{-1}, and wind direction of 0 - 360° with an accuracy of $\pm$ 0.1° and a resolution of 0.1°. It was set at 70 cm above the plane of the propellers of the UAV, mounted on a custom-design carbon fiber tube and frame which was further mounted onto a rectangular carbon fiber support base attached to the underbelly of the UAV body, to minimize the effect of propellers-induced flow on the anemometer measurement. The x_t-y_t-z_t coordinate axes of the anemometer, with its center as the origin, were set to be parallel to the x-y-z axes of the aircraft body frame. The mounting of the three-dimensional anemometer is shown in Fig. 1(a).

A base digital model of the UAV was provided by its manufacturer for the present CFD simulations. The digital model was further augmented with the accurate digital representation of the three-dimensional anemometer and its mounting frame. Furthermore, considering that the UAV wind measurements are usually tied to other air measurement applications, necessitating additional payload attached to the UAV underbelly simultaneously. Such a payload on the UAV needs also to be included in the digital model for the CFD simulation. In the present case, we added the digital model of a 6.37 kg air sampler developed in our group (Yang et al., 2024) to the UAV base digital model (Fig. 1(b)).

~~For CFD simulations, the complete digital model for the UAV and its payloads was set in the x_s-y_s-z_s simulation coordinate system in Solidworks, a computational fluid simulation tool, on a one to one scale (Fig. 1(b)).~~
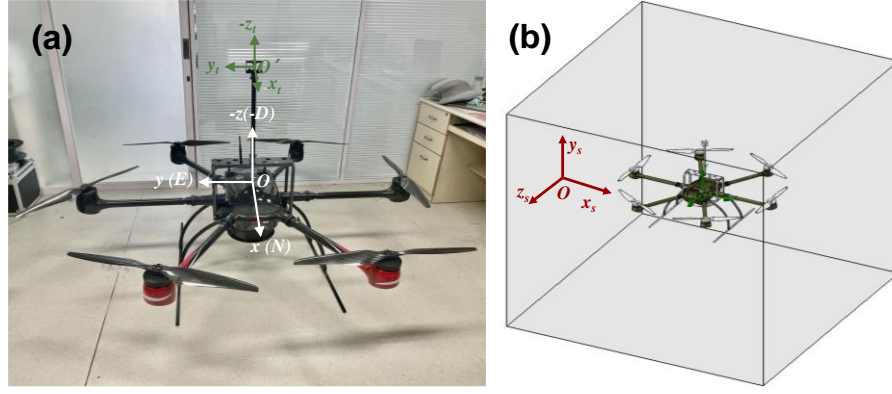
Figure 1: The establishment of the coordinate system and numerical simulation model for the UAV wind measurement platform. (a) The UAV wind speed measurement platform. (b) The digital model of the UAV wind measurement platform in the 3D CFD model simulation domain.

2.1.2 Simulation Tool

The CFD simulations were conducted using SolidWorks Flow Simulation 2022, a pressure-based finite volume solver employing a fully coupled turbulence modeling approach. It employs an adaptive Cartesian mesh approach for three-dimensional solid meshing, with the governing equations being the Navier-Stokes equations for simulating the interaction of fluids, and the turbulence model utilizing the standard k-ε two-equation model (Jonuskaite, 2017).

The selection of SolidWorks Flow Simulation was driven by its seamless integration with CAD geometries, which eliminated potential errors associated with STL file conversions for our complex multi-rotor UAV design. Additionally, its wall functions for boundary layers effectively resolve gradient variations in boundary layers around rotating blades, reducing trial and error related to near-wall settings. The built-in solver convergence adopts a phased approach to multiple variant scenarios, decreasing the need for re-runs caused by insufficient convergence and thereby conserving computational costs. Its unique turbulence model automatically determines flow regimes (laminar, transitional, and turbulent), ensuring shorter turbulence model setup times while maintaining enhanced model accuracy (Azmi et al., 2017; Ramya et al., 2015).

While ANSYS Fluent offers advanced transient turbulence models (e.g., DES/LES), its computational cost for equivalent spatial resolution was typically higher than SolidWorks (Afaq and Ahmad, 2023). Given our need to simulate over 100 operational scenarios, SolidWorks' balance of engineering accuracy and computational tractability was deemed optimal for deriving empirical correction algorithm.

For CFD simulations, the complete digital model for the UAV and its payloads was set in the x_s-y_s-z_s simulation coordinate system in Solidworks, on a one-to-one scale (Fig. 1(b)).

2.2 Simulation Scenarios

For the UAV flight simulation, we considered over a hundred flight envelope scenarios, including parameters such as UAV flight altitude, wind direction, and wind speed. Since the UAV's predominant flights are within the atmospheric boundary layer, characterized by significant variability in wind speed and directions, a flight envelope for the UAV in the simulated environments was setup for the complete UAV digital model for flight altitudes of 30 and 1000 meters, respectively. The lower height (30 m) represents the typical operational altitude for industrial UAV applications within the boundary layer, while the upper height (1000 m) corresponds to the altitude where atmospheric flow transitions to more stable, low-density free-stream conditions. These flight envelopes were designed for the UAV to subject to headwind, tailwind, and crosswind relative to its flight direction. Under the constraint that the UAV can only operate under true wind speeds ≤ 18 m s^{-1}, and assuming the applicability of the correction algorithm to most flight scenarios, CFD simulations were conducted for the UAV under these three wind directions. The simulations encompassed the following flight envelopes as listed in Table 1: the UAV flew at ground speeds of 18, 14, 10, and 8 m s^{-1}, respectively, and adapted to wind speeds of 1.5, 3.3, 5.4, 7.9, 10.7, and 14 m s^{-1}. It should be noted that the numerical simulations were conducted by converting wind speed and ground speed into airspeed through vector synthesis.

Table 1: The simulation flight envelope scenarios for the UAV-based wind measurement platform.

Wind Type	Ground Speed (m s^{-1})	Wind speed (m s^{-1})	Wind Type	Ground Speed (m s^{-1})	Wind speed (m s^{-1})	Wind Type	Ground Speed (m s^{-1})	Wind speed (m s^{-1})
		1.5			1.5			1.5
		3.3			3.3			3.3
	8	5.4		8	5.4		8	5.4
		7.9						7.9
		10.7						10.7
Tailwind			Headwind			Crosswind		14
		1.5			1.5			1.5
		3.3			3.3			3.3
	10	5.4		10	5.4		10	5.4
		7.9			7.9			7.9
		10.7						10.7

					14
	1.5		1.5		1.5
	3.3		3.3		3.3
14	5.4	14	5.4	14	5.4
	7.9		7.9		7.9
	10.7		10.7		10.7
					14
	1.5		1.5		1.5
	3.3		3.3		3.3
18	5.4	18	5.4	18	5.4
			7.9		7.9
			10.7		10.7
			14		14

2.3 Flight Parameters

The movements of the UAV through air, including takeoff, ascent/descent, attitude changes, turning, and horizontal flights, are driven by the rotary propellers, whose power requirement is closely tied to the weights of the UAV and its payload as well as the relative motions of the UAV in air. During a normal flight, the UAV adjusts its inclination angle and propeller speeds in order to achieve a set ground speed for flight. By analyzing the gravity G, pull T and wind resistance D experienced by the UAV under flight conditions (Fig. 2), its inclination angle θ and propeller rotation speed M can be calculated according to Eqs. (1) - (5) (Quan, 2017).

Figure 2: Schematic diagram of forces acting on a UAV.

$$\tan\theta \times mg = D, \tag{1}$$

$$p \times (\sin\theta \times S_{xoy} + \cos\theta \times S_{xoz}) = D, \tag{2}$$

$$0.5\rho(V_{wind} + V_{UAV})^2 = p, \tag{3}$$

$$\cos\theta \times mg = T, \tag{4}$$

201 $$T = C_T \times \rho \times \left(\frac{M}{60}\right)^2 \times D_p^{\;4}, \tag{5}$$

202 where θ is the inclination angle of the UAV; m is the combined weight of the UAV and the payloads (i.e,

203 the air sampler and the anemometer along with its installation frame in the present case), calculated to

204 be 28.869 kg; g is the gravitational constant at 9.8 m s^{-2}; D is the wind resistance in Newtons; V_{wind} is

205 the wind speed in m s^{-1}; V_{UAV} is the ground speed of the UAV in m s^{-1}; p is the wind pressure on the UAV

206 in N/m^2; S_{xoy} and S_{xoz} are the projected surfaces of the UAV in the horizontal direction and vertical

207 directions, determined to be 0.296 and 0.229 m^2, respectively; C_T is the rotor pull coefficient with an

208 experimentally determined value of 0.048542; D_p is the UAV propeller diameter at 0.8128 m; ρ is the

209 air density in kg m^{-3}; T is each rotor pull in Newton; M is the rotation speed of the rotors in RPM.

210 The complete flight envelope was defined by combinations of critical parameters, ~~Each set of flight~~

211 ~~condition parameters that constitute the full flight envelope,~~ including wind directions, wind speeds,

212 airspeeds, ground speed, inclination, wind resistance, pull, and M-. A series of CFD simulations were

213 conducted to systematically evaluate the simulated wind field characteristics for each unique parameter

214 set within this envelope.~~The CFD simulations were performed to determine the simulated wind fields~~

215 ~~for each set of parameters in the flight envelope one at a time.~~

216 **2.4 Simulation Parameters**

217 The simulation parameters primarily include the computational domain and mesh, fluid and

218 environmental properties, as well as the rotating region. During the CFD flow simulations of the UAV

219 using Solidworks, the computational domain dimensions (3.3 × 3.3 × 3.3 m³) were determined by

220 prioritizing the analysis of flow field distribution around the anemometer while balancing computational

221 costs.~~the computational domain was set to 3.3 × 3.3 × 3.3 m³ according to the wingspan of the UAV,~~

222 ~~with the complete UAV plus payload digital model set at the center of the domain.~~ The computational

223 domain was divided into two parts with different spatial resolutions based on the grid sizes,considering

224 the computational time and accuracy required for resolving the details of the digital UAV model. The

225 first part was the global domain with a grid size of 0.23 × 0.23 × 0.23 m³, providing a lower spatial

226 resolution. The second part was a nested subdomain within the global domain, specifically defined for

227 the position and dimensions of the anemometer to simulate the measured velocities. The grid size for

228 this nested subdomain was set at 0.0125 × 0.0125 × 0.0125 m³, providing a higher spatial resolution.

229 The total number of grids in the computational domain was 1.11×10^8, and the specific grid configurations

230 are shown in ~~the~~ Fig. ~~2~~3. The wall is set as an adiabatic wall, and its roughness is set to 0. The fluid was

231 modeled as air with characteristics of turbulent and laminar flow. To isolate the rotor-induced flow

232 dynamics from background atmospheric turbulence, a turbulence intensity of 0.1% and a turbulence

233 length scale of 0.012 m were set. This low turbulence intensity minimizes confounding effects from

234 ambient atmospheric fluctuations, while the length scale corresponds to the anemometer frame width

235 (~0.01 m) to resolve rotor-generated eddies. These assumptions prioritize the systematic bias correction

236 for rotor-induced airflow. ~~, with a turbulence intensity of 0.1% and a turbulence length scale of 0.012 m.~~

237 The atmospheric pressure was adjusted to 1.01×10^5 and 9.00×10^4 Pa at altitudes of 30 m and 1000 m,

238 respectively, and the atmospheric temperature was assumed to be 25 °C at both altitudes. The relative

239 humidity at different altitudes was determined based on the prescribed pressure and temperature

240 corresponding to each altitude. The detailed configurations of these parameters are listed in Table 2.

241  The UAV's airspeed and aerodynamic angles were configured according to the different flight

242 parameters described in Sect. 2.2 and 2.3. To represent the rotor digitally, six virtual cylinders of the

243 same volume were used to encapsulate the six rotors, with their circumferences match the rotating

244 trajectory of the propeller tip. These virtual cylinders were treated as the rotational regions in the CFD

245 simulation, with their rotation directions aligned with the actual rotation direction of the UAV's

246 propellers. The rotation direction from rotor No. 1 to 6 was alternately clockwise and counterclockwise,

247 and the rotation speed for each flight condition was obtained from Eqs. (1) - (5).

248
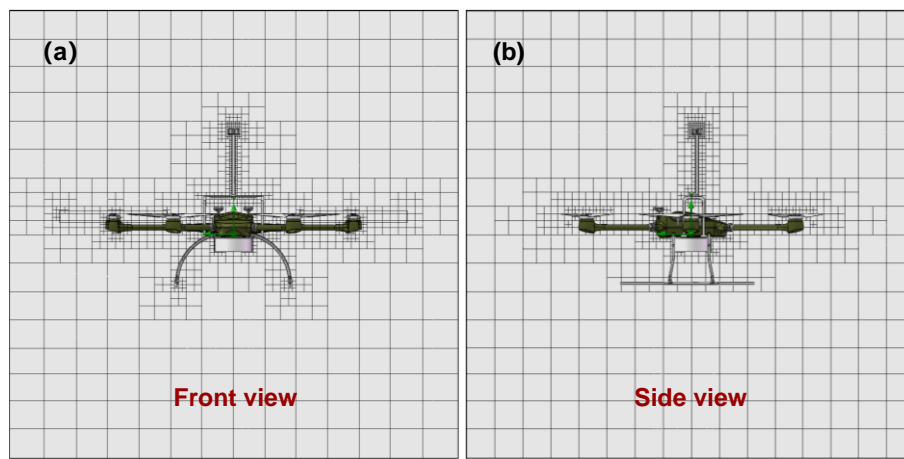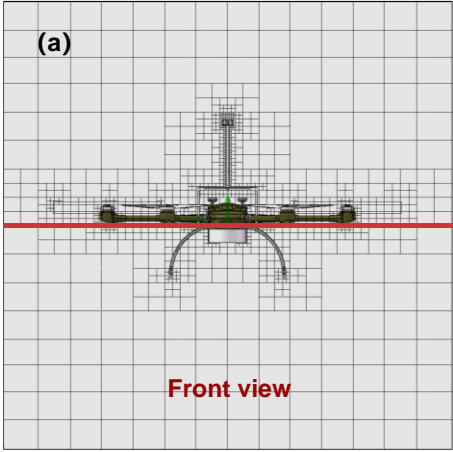
249 **Figure 3: Grid configuration of the computational domain.**

250 **Table 2: Simulation parameters configuration.**
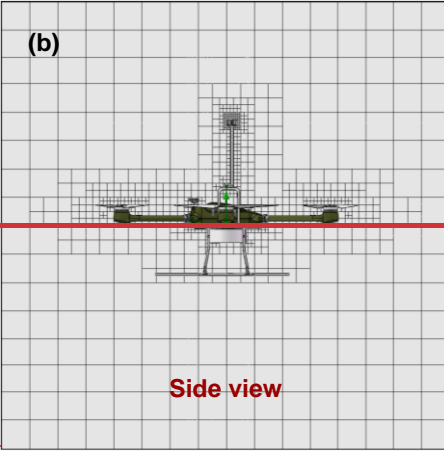
Parameters	Content
Computational domain size	$3.3 \times 3.3 \times 3.3$ m³
Global domain grid size	$0.23 \times 0.23 \times 0.23$ m³
Subdomain grid size	$0.0125 \times 0.0125 \times 0.0125$ m³
Total number of computational domain grids	1.11×10^8
Turbulence intensity	0.1%
Turbulence length scale	0.012 m
Roughness	0
30 m atmospheric pressure	1.01×10^5 Pa
1000 m atmospheric pressure	9.00×10^4 Pa
30 m atmospheric temperature	25 °C
1000 m atmospheric temperature	25 °C

Figure 2: Grid configuration of the computational domain.

To ensure relatively accurate simulations, two categories of flow field properties were specified as computational objectives prior to the start of the simulations, and the simulations were terminated upon convergence of the simulation results for all objectives. The first category comprised global domain computational objectives, including average total pressure (P_G), average velocity (V_G), average vertical velocity (V_{Gy}), and average forward velocity (V_{Gz}), where the subscript G denotes the global domain. The second category consisted of subdomain computational objectives, which included the average velocity (V_S), three-dimensional average speed components V_{Sx}, V_{Sy} and V_{Sz} at the anemometer position in the simulation coordinate system. It is noteworthy that the aforementioned average values refer to the spatial averages over the global domain or subdomain.

Upon simulation completion, these velocity components (V_{Sx}, V_{Sy}, V_{Sz}) were further converted to velocity components at the anemometer sensor position (u_{x_sensor}, u_{y_sensor}, u_{z_sensor}) in the airframe coordinate according to the coordinate system shown in Fig. 1((a) and (b)) and Eqs. (6) - (8) below. The converted velocities, u_{x_sensor}, u_{y_sensor}, u_{z_sensor}, were subtracted from the airspeed~~wind velocity~~ (denoted

266 as u_{x_air}, u_{y_air}, and u_{z_air}) setting for each CFD simulation, to estimate the false wind signals arising

267 from the induced flow by the UAV rotors, expressed with Δu_x, Δu_y and Δu_z, respectively, using Eqs.

268 (9) - (11).

269 $$u_{x\_sensor} = -Vs_z, \tag{6}$$

270 $$u_{y\_sensor} = Vs_x, \tag{7}$$

271 $$u_{z\_sensor} = -Vs_y, \tag{8}$$

272 $$\Delta u_x = u_{x\_sensor} - u_{x\_air}, \tag{9}$$

273 $$\Delta u_y = u_{y\_sensor} - u_{y\_air}, \tag{10}$$

274 $$\Delta u_z = u_{z\_sensor} - u_{z\_air}, \tag{11}$$

275 In other words, the false wind signals Δu_x, Δu_y and Δu_z are the terms that must be determined and

276 corrected for in the wind measurements from the UAV.

277 **3 Result and Discussion**

278 **3.1 Example Analysis of Simulation Results**

279 According to the Sect. 2.2, this study develops a series of simulation scenarios for the UAV digital

280 model under various combinations of altitude (30 and 1000 m), wind direction (tailwind, headwind, and

281 crosswind), ground speed (8 to 18 m/s), and wind speed (1.5 to 14 m/s). To demonstrate the flow field

282 characteristics around the UAV under various scenarios, one UAV hovering scenario and Six six

283 representative simulation scenarios were specifically selected for analysis as examples.

284 Fig. 4 presents the cross-sectional view of the velocity flow field around the UAV in a hovering

285 state under wind-free conditions. In this scenario, the surrounding velocity field is solely generated by

286 the rotational induced flow from the UAV's own rotors. The simulated 2-4 m/s airflow around the

287 anemometer originates exclusively from rotor rotation, demonstrating that the rotor-induced flow during

288 hovering inherently interferes with wind speed measurements by the anemometer.
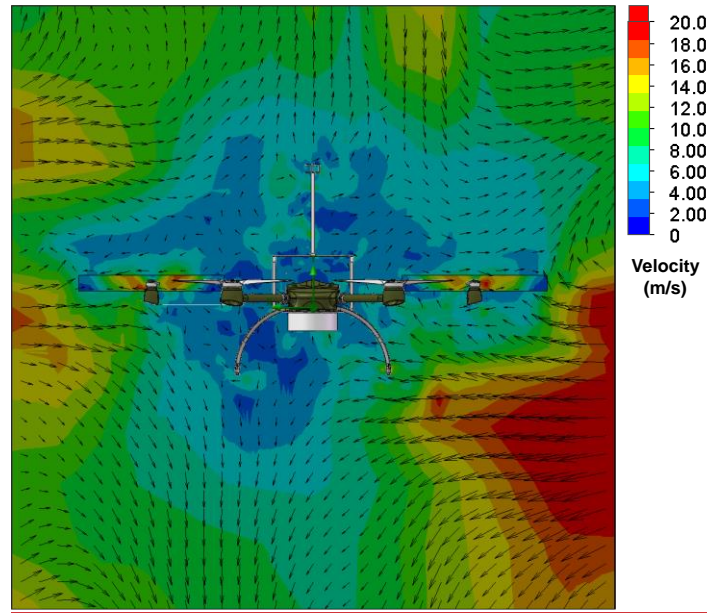
Figure 4: The velocity flow field distribution of the UAV's hovering state.

The other six~~These~~ scenarios include UAV flight simulations at altitudes of 30 m and 1000 m, with a ground speed of 8 m/s and a wind speed of 5.4 m/s, under tailwind, headwind, and crosswind conditions. Fig. ~~3~~5 to ~~5~~7 present cross-sectional views of the surrounding flow fields during UAV flight under these conditions. In the figures, color gradients represent the magnitude of the velocity, while arrows indicate both the direction and magnitude of the velocity. Overall, under varying wind conditions, the direction and speed of airflow around the UAV show significant differences. While the airflow direction around the UAV remains relatively consistent at the both simulation altitudes, the airflow speed at 1000 m is slightly higher than at 30 m, particularly under tailwind conditions. Specifically, based on the ground speed, wind direction, and wind speed settings, the UAV's airspeed relative to the wind is 2.6 m/s, 13.4 m/s, and 5.4 m/s in tailwind, headwind, and crosswind scenarios, respectively.

As show in Fig. ~~3~~5 (a) and (b), in the tailwind scenario, the maximum downwash velocity occurs directly beneath the UAV rotors, with the airflow directed vertically downward. The next highest velocities are observed around the sides and above the rotors, where the airflow follows an inward and downward trend. The wind speed at the anemometer location is minimally influenced by the UAV rotors, meaning the measured wind speed represents the true airspeed. In the headwind scenario (Fig. ~~4~~6 (a) and (b)), the highest airflow velocity is detected near the area directly above the rotors, with the airflow also following an inward and downward pattern. The lowest velocity is found directly below the rotors, where the airflow moves upward and outward. At the anemometer's location, some interference from

the UAV rotors is present, so the wind speed at this point is a combination of the true airspeed and the

rotor-induced velocity. As exhibited in Fig. 5 7 (a) and (b), in the crosswind scenario with wind blowing

from left to right, the airflow around the UAV resembles that in the headwind scenario, but the overall

flow field is deflected to the right due to the crosswind, with relatively lower airflow velocity. In the

scenario with wind blowing from right to left, the flow field shifts to the left.

These simulation results show that the flow field around the UAV varies significantly depending

on both the presence/absence of wind and its directional characteristicswind direction, and the

anemometer experiences different levels of interference accordingly. Thus, accurately quantifying the

interference of the UAV rotors on the anemometer is essential. However, in practical application

scenarios, it is also necessary to comprehensively consider additional airflow disturbances induced by

the UAV's own motion and attitude fluctuations, and to develop corresponding dynamic compensation

algorithms.
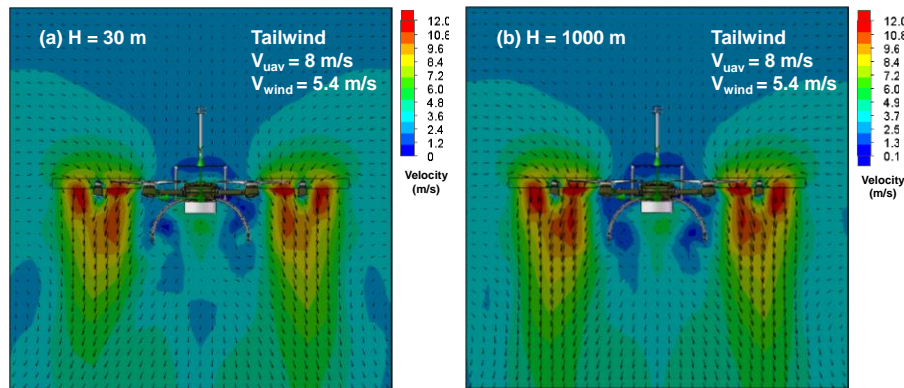
Figure 35: Simulation flow field example results of the UAV wind measurement platform in the tailwind scenario. (a) and (b) represent the longitudinal cross-sections of the simulation flow fields for the UAV at altitudes of 30 m and 1000 m, with a ground speed of 8 m/s and a wind speed of 5.4 m/s.
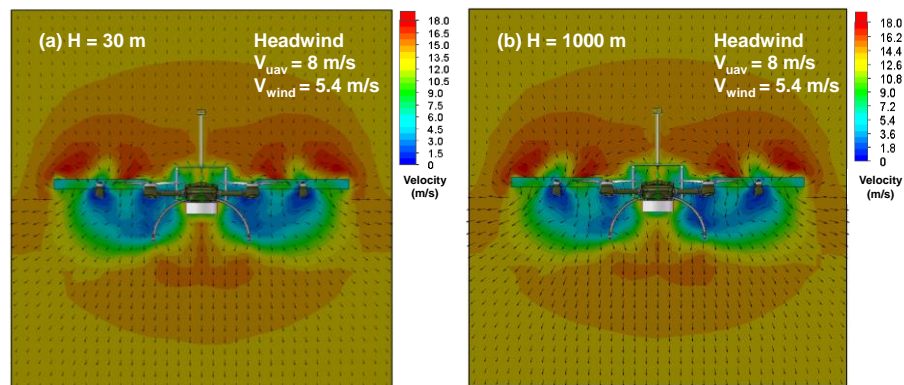
Figure 46: Simulation flow field example results of the UAV wind measurement platform in the headwind scenario. (a) and (b) represent the longitudinal cross-sections of the simulation flow fields for the UAV at altitudes of 30 m and 1000 m, with a ground speed of 8 m/s and a wind speed of 5.4 m/s.
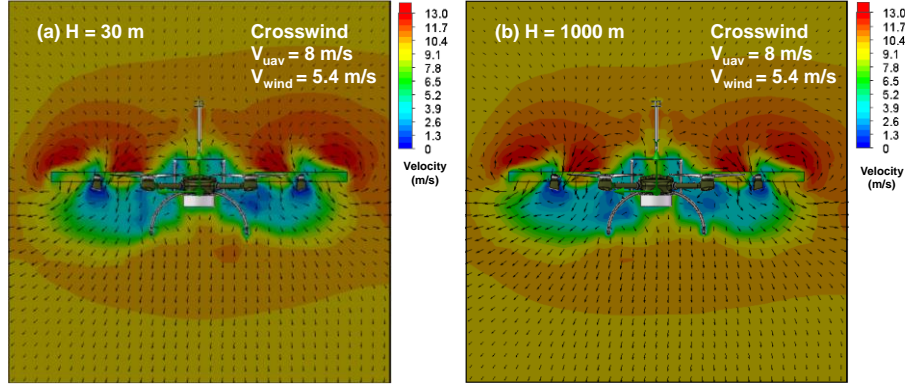
Figure 5̶7̶: Simulation flow field example results of the UAV wind measurement platform in the crosswind scenario. (a) and (b) represent the longitudinal cross-sections of the simulation flow fields for the UAV at altitudes of 30 m and 1000 m, with a ground speed of 8 m/s and a wind speed of 5.4 m/s.

3.2 The effect of flight altitude on rotor interference with anemometer measurements

Through simulating the flight of UAV in all simulation scenarios, the false signals produced by the UAV rotors on the anemometer at different altitudes and wind characteristics were captured. Initially, the influence of flight altitude on the false signals was examined.

The simulated flight data under tailwind and headwind conditions were integrated into a unified data set since the UAV flight velocity vector is parallel to the tailwind and headwind velocity vectors during normal flight. The simulated false wind signals on the anemometer in the airframe x, y, and z directions, caused by the propeller induced airflow under tailwind and headwind conditions, were represented by $\Delta u_x^{T/HW}$, $\Delta u_y^{T/HW}$, and $\Delta u_z^{T/HW}$, respectively. For the tailwind and headwind datasets, according to the Wilcoxon non-parametric test for paired samples, as shown in ~~Table 2~~Table 3, the differences in $\Delta u_x^{T/HW}$, $\Delta u_y^{T/HW}$ and $\Delta u_z^{T/HW}$ were not significant ($p < 0.05$) at either the 30 m or the 1000 m altitudes. Therefore, in the presence of tailwind or headwind, the interference from the UAV propeller-induced flow on the anemometer measurement can be considered independent of the flight altitude in this altitude range.

Similarly, the simulated false wind signals for the crosswind conditions on the anemometer in the x, y, and z directions were represented by Δu_x^{CW}, Δu_y^{CW}, and Δu_z^{CW}. The Wilcoxon non-parametric test of paired samples was also applied (shown in Table 1) between the two altitudes. No significant differences were found for Δu_x^{CW}, Δu_z^{CW} between the two altitudes, but there was an obvious discrepancy for Δu_y^{CW} ($p = 0.00$)at the two altitudes. This indicates that under cross wind conditions, the disturbances of the UAV propeller in the x and z directions of the anemometer are not altitude

dependent, but that in the y ~~(upward)~~ direction it is necessary to distinguish the altitude. This behavior can be attributed to differences in the interaction between the y direction component and rotor rotational momentum caused by variations in atmospheric density at different altitudes under crosswind conditions.

~~Table 2~~Table 3: Wilcoxon nonparametric tests for paired samples of false wind velocity signals between 30 m and 1000 m flight altitudes.

Wind Types	False Wind Signal	Significance	α	Test results
Tailwind/Headwind	$\Delta u_x^{T/HW}$	0.93	0.05	No difference
	$\Delta u_y^{T/HW}$	0.72	0.05	No difference
	$\Delta u_z^{T/HW}$	0.21	0.05	No difference
Crosswind	Δu_x^{CW}	0.36	0.05	No difference
	Δu_y^{CW}	0.00	0.05	Significant difference
	Δu_z^{CW}	0.81	0.05	No difference

3.3 Rotor Interference on Anemometer Measurements

This study employs a regression fitting to explore the relationship between the false wind signals generated by the UAV rotors airflow and the UAV's airspeed. Under tailwind and headwind conditions, the false wind signals ($\Delta u_x^{T/HW}$, $\Delta u_y^{T/HW}$, and $\Delta u_z^{T/HW}$) on the anemometer resulting from the UAV rotor -induced flows at both flight altitudes were aggregated and fitted as dependent variables in a regression using u_{x_sensor} as the independent variable. As shown in Fig. ~~6~~8 (a), (b) and (c), good linear relationships were found between $\Delta u_x^{T/HW}$, $\Delta u_y^{T/HW}$, and $\Delta u_z^{T/HW}$ and the simulated velocity components in the x-direction (u_{x_sensor}), respectively. The specific relationship is described by Eqs. (12) to (14). Thus, using the UAV velocity components in x direction, the false wind signals caused by the UAV propellers can be determined and removed from the raw measured wind velocity from the anemometer.

For crosswind conditions, regressions were fitted with false wind signals (Δu_x^{CW} and Δu_z^{CW}) as dependent variables and u_{x_sensor} as the independent variable in the same way (See Fig. ~~7~~9). A linear relationship was observed between the false wind signals in both x and z directions (Δu_x^{CW} and Δu_z^{CW}) and u_{x_sensor}, with the specific expressions in Eq. (15) and (16), respectively. As described in Sect. 3.2, Δu_y^{CW} was sensitive to flight altitude under crosswind conditions, hence Δu_y^{CW} at 30 m and 1000 m

374 altitude ($\Delta u_{y(30)}^{CW}$ and $\Delta u_{y(1000)}^{CW}$) were regressed against u_{y_sensor} for the two flight altitudes

375 separately. The $\Delta u_{y(30)}^{CW}$ exhibited a linear relationship with u_{y_sensor}, as shown in Eq. (17). However,

376 the correlation coefficient between $\Delta u_{y(1000)}^{CW}$ and u_{y_sensor} was found to be lower than 0.5, indicating

377 that $\Delta u_{y(1000)}^{CW}$ may be considered independent of u_{y_sensor}. Therefore, the average value of $\Delta u_{y(1000)}^{CW}$

378 (0.006 m s^{-1}) was regarded as the $\Delta u_{y(1000)}^{CW}$ at this flight altitude.

379 Despite the dependence of Δu_y^{CW} on flight altitudes, $\Delta u_{y(30)}^{CW}$ and $\Delta u_{y(1000)}^{CW}$ are confined to a

380 similar numeric range. Therefore, they may be roughly considered as representing Δu_y for lower

381 altitude (e.g., 0 to 500 m) and higher altitude (e.g., 500 to 1000 m), respectively.

382 Hence, for crosswind situations, the wind velocities in the x, y and z directions measured by the

383 anemometer are corrected by subtracting Δu_x^{CW}, Δu_z^{CW} and $\Delta u_{y(0-500)}^{CW}$ which are estimated from

384 $u_{x\_sensor}/u_{y\_sensor}$, or at relatively high flight altitudes using a constant value of 0.006 m s^{-1} for

385 $\Delta u_{y(501-1000)}^{CW}$.

386
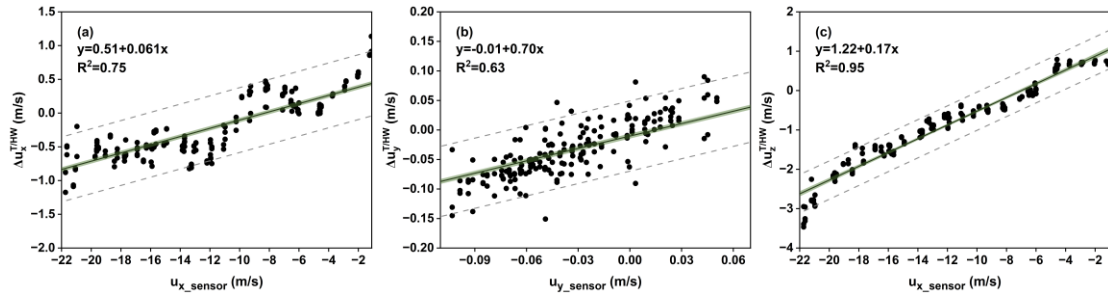
Figure 6̶8̲: Regression fit of artificial velocity ($\Delta u_x^{T/HW}$, $\Delta u_y^{T/HW}$ and $\Delta u_z^{T/HW}$) with u_{x_sensor} for tailwind
and headwind flight conditions at two altitudes. In the figure, simulation data are marked with black dots,
fitted curves are indicated in black lines, the 95% confidence bands are identified as green shadows, and the
95% prediction bands are represented with gray dashed area.

391
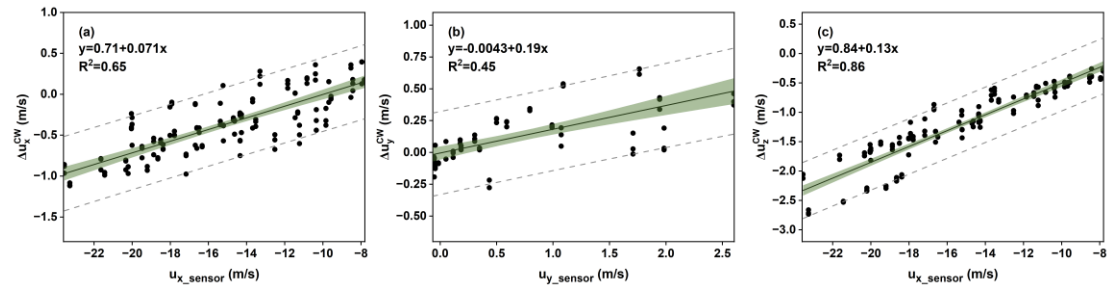
Figure 7̶9̲: Regression fit of false wind velocity signals Δu_x^{CW}, Δu_z^{CW} and $\Delta u_{y(0-500)}^{CW}$ with $u_{x\_sensor}/$
u_{y_sensor} for crosswind flight conditions at two altitudes. The symbols in the figure are the same as in Figure
6.

395 $$\Delta u_x^{T/HW} = 0.51 + 0.061 \times u_x, \tag{12}$$

396 $\Delta u_y^{\text{T/HW}} = -0.01 + 0.70 \times u_y,$ (13)

397 $\Delta u_z^{\text{T/HW}} = 1.22 + 0.17 \times u_x,$ (14)

398 $\Delta u_x^{\text{CW}} = 0.71 + 0.071 \times u_x,$ (15)

399 $\Delta u_z^{\text{CW}} = 0.84 + 0.13 \times u_x,$ (16)

400 $\Delta u_{y(0-500)}^{\text{CW}} = -0.0043 + 0.19 \times u_y, \quad (h = 0 \sim 500 \text{ m}),$ (17)

401 $\Delta u_{y(501-1000)}^{\text{CW}} = 0.006, \quad (h = 501 \sim 1000 \text{ m}),$ (18)

402   In Eq. (17) and (18), the variable h represents the flight altitude of the UAV.

403 **3.4 The Overall Correction Algorithm**

404 **3.4.1 Motion and Attitude Compensation Correction of UAV**

405   In addition to the false wind signals caused by propeller rotations, additional false wind velocity

406 signals from the anemometer can be attributed to UAV movement and attitude (pitch, roll and yaw)

407 changes during flight, and as such also need correction. When the UAV moves horizontally and vertically

408 relative to the ground, the velocity vector measured by the anemometer is a vector combination of the

409 true wind velocity and the UAV's ground velocity. Consequently, the ground velocity of the UAV (v_x and

410 v_z, with v_y always 0 due to no motion in the y direction) contributes false wind velocity components to

411 measurements by the anemometer. Moreover, the UAV's flight attitude undergoes adjustments in the

412 pitch, roll, and yaw Euler angles (θ, φ, and ψ, respectively), in order to compensate for aerodynamic

413 resistance or adapt to flight plans. These adjustments lead to the anemometer measuring additional

414 velocities resulting from the rotational rates of the attitude angles ($\mu(\theta)$ and $\mu(\varphi)$, with $\mu(\psi)$

415 remaining zero due to the alignment of the rotational axis of ψ with the line connecting the UAV's center

416 of gravity and the anemometer. Furthermore, the effect is further amplified by the distance (r) between

417 the anemometer and the UAV's center of gravity. It is noteworthy that there is currently no reported

418 correction algorithm for influence of attitude angle variations on anemometer wind velocity

419 measurements from UAVs. To obtain accurate wind information, after eliminating the aforementioned

420 interferences, the wind velocities (u_x, u_y and u_z) observed by the anemometer in the airframe coordinate

421 (x, y and z directions) were transformed to the North-East-Down (NED) ground coordinate using the

422 direction cosine matrix (DCM) as given in Eq. (19).

423 $\begin{bmatrix} u_N \\ u_E \\ u_D \end{bmatrix} = \text{DCM}(\theta, \varphi, \psi) \left(\begin{bmatrix} u_x \\ u_y \\ u_z \end{bmatrix} + \begin{bmatrix} v_x \\ 0 \\ -v_z \end{bmatrix} + \begin{bmatrix} \mu(\theta) \\ -\mu(\varphi) \\ 0 \end{bmatrix} \right),$ (19)

424

$$DCM(\theta, \varphi, \psi) = \begin{bmatrix} \cos(\psi) & -\sin(\psi) & 0 \\ \sin(\psi) & \cos(\psi) & 0 \\ 0 & 0 & 1 \end{bmatrix} \begin{bmatrix} \cos(\theta) & 0 & \sin(\theta) \\ 0 & 1 & 0 \\ -\sin(\theta) & 0 & \cos(\theta) \end{bmatrix} \begin{bmatrix} 1 & 0 & 0 \\ 0 & \cos(\varphi) & -\sin(\varphi) \\ 0 & \sin(\varphi) & \cos(\varphi) \end{bmatrix}, \quad (20)$$

425 where DCM is defined by Eq. (20); u_N, u_E and u_D refer to corrected North, East and Down

426 components of wind velocity in the ground coordinate; v_x and v_z are the motion velocities of the UAV

427 in the x and z directions respectively, which are directly provided by the GPS receiver output of the

428 UAV or can be directly computed from the UAV longitude/latitude coordinate output; $\mu(\theta)$ and $\mu(\varphi)$

429 represent the product of the pitch rate $\omega(\theta)$ and roll rate $\omega(\varphi)$, respectively, with the rotation radius r,

430 which is the distance between the anemometer and the center of gravity of the UAV, as defined in Eqs.

431 (21) and (22). Due to the alignment of the anemometer's z-axis with that of the UAV, the variation in

432 yaw ψ does not introduce false wind speed to signals from the anemometer in the airframe coordinate,

433 resulting in μ(ψ) being equal to zero.

434 $$\mu(\theta) = \omega(\theta) \times r = \frac{d(\theta)}{dt} \times r, \tag{21}$$

435 $$\mu(\varphi) = \omega(\varphi) \times r = \frac{d(\varphi)}{dt} \times r, \tag{22}$$

436 where $\omega(\theta)$ and $\omega(\varphi)$ are defined as the differentiation of θ and φ with respect to time t,

437 respectively.

438 **3.4.2 Compensation Correction for Induced-Flow Disturbance by UAV Rotors**

439 Based on the statistical analyses of the fluid simulation results in Sect. 3.3, the regression

440 relationships between the false wind velocity signals generated by the propeller rotation and the

441 simulated wind components sensed by the anemometer are integrated into the motion and attitude

442 correction algorithm of UAV given in Eq. (19). The updated wind velocity correction algorithm is given

443 as Eq. (23), whose second and third vectors on the right side of Eq. (23) represent the contributions of

444 the propeller-induced wind signals under tailwind/headwind and crosswind conditions to u_x, u_y and u_z,

445 respectively, with A and B defined in Eqs. (~~17~~24) and (~~18~~25) to quantify their magnitudes. Since the

446 measured wind velocities u_x and u_y from the anemometer correspond to the simulated u_{x_sensor} and u_{y_sensor},

447 respectively, the regression relationships are modified by replacing u_x and u_y with u_{x_sensor} and u_{y_sensor},

448 respectively. This yields the estimations of the false wind velocity signals, Δu_x, Δu_y and Δu_z, under

449 different wind directions, in relation to u_x and u_y, as specified by Eqs. (12) - (18). Using Eq. 16, the actual

wind velocity components, including north wind (u_N), east wind (u_E), and vertical wind (u_D), are computed after correcting for the effects of UAV's rotor propeller disturbance, motion, and attitude on the wind signal measurements from the anemometer.

$$\begin{bmatrix} u_N \\ u_E \\ u_D \end{bmatrix} = \text{DCM}(\theta, \varphi, \psi) \left(\begin{bmatrix} u_x \\ u_y \\ u_z \end{bmatrix} - \begin{bmatrix} A \times \Delta u_x^{T/HW} \\ A \times \Delta u_y^{T/HW} \\ A \times \Delta u_z^{T/HW} \end{bmatrix} - \begin{bmatrix} B \times \Delta u_x^{CW} \\ B \times \Delta u_y^{CW} \\ B \times \Delta u_z^{CW} \end{bmatrix} + \begin{bmatrix} v_x \\ 0 \\ v_z \end{bmatrix} + \begin{bmatrix} -\mu(\theta) \\ \mu(\varphi) \\ 0 \end{bmatrix} \right) , \tag{23}$$

$$A = \left| \frac{u_x}{\sqrt{u_x{}^2 + u_y{}^2}} \right|, \tag{24}$$

$$B = \left| \frac{u_y}{\sqrt{u_x{}^2 + u_y{}^2}} \right|, \tag{25}$$

3.5 Validation of the Correction Algorithm

A comparative experiment was designed to verify the effectiveness of the correction algorithm described in Eq. (23). The experiment primarily compares three different wind data: the first is the three-dimensional wind vector corrected only for UAV motion and attitude compensation (Eq. (19) and denoted as $\mathbf{V_O}$), the second includes additional corrections for UAV rotor interference, along with motion and attitude compensation (Eq. (23) and denoted as $\mathbf{V_R}$), and the third is the three-dimensional wind directly measured by the meteorological tower (denoted as $\mathbf{V_T}$). The comparison experiment was conducted with the UAV flying wind-boxes around the 80-meter meteorological tower within the Experimental Base of the Beijing Key Laboratory of Cloud, Precipitation and Atmospheric Water Resources. The meteorological tower was equipped with three-dimensional ultrasonic anemometers positioned at heights of 30, 50, and 70 m, with one anemometer in the north and one in the south (see Fig. 810). Experiments were conducted during the daytime on July 19, 2022, with neutral atmospheric stability to minimize thermal boundary layer effects on vertical wind variability.

The UAV flew around the tower in a box flight path at a horizontal distance of about 10 m away from the tower, at all three heights. During these flights, the UAV maintained a commanded horizontal speed of approximately 5 m/s, a value selected as a compromise between achieving sufficient spatial sampling resolution and maintaining stable flight attitude control. A total of 30 independent wind-box flights were conducted, with each altitude (30, 50 m and 70 m) sampled 10 times. Each flight lasted

475 approximately 13 minutes, generating over 800 valid data points per altitude. Given the potential

476 interference from near-surface vegetation on the 30-meter anemometer on the tower, wind velocities

477 acquired by the UAV at 50 and 70 m heights during steady flight intervals were analyzed herein. Using

478 a 3σ threshold of the mean value of the entire dataset to exclude data outliers caused by sudden gusts

479 or UAV maneuvers (such as turning), retaining data during steady UAV flight periods.

480
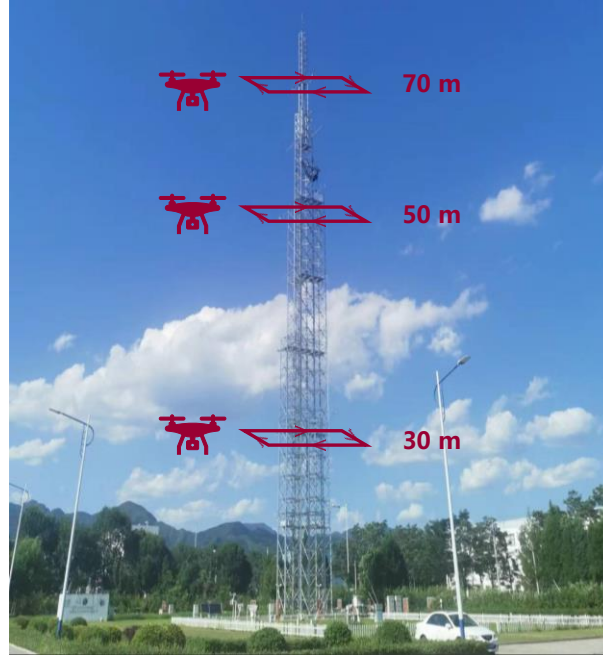
481
482 **Figure 8̶10: Comparative experiment on wind measurements between the UAV and the meteorological tower.**

483 Fig. 11 presents the V_O, V_R, and V_T time-series data acquired during the dual-altitude flight tests

484 of the UAV at 70 m and 50 m, with the 70 m altitude test data collected prior to 15:05 and the 50 m

485 altitude test data obtained after 15:10. The results in Fig. 9̶11 (a) demonstrate that at elevated wind

486 speeds (> 3 m s^{-1}), the wind velocities of V_R were substantially lower than that of V_O. The root mean

487 square relative errors between V_R and V_T, and V_O and V_T, are 0.28 and 0.37, respectively, with the

488 former being approximately 24% smaller than the latter. This indicates that the correction effect of Eq.

489 (23) is especially pronounced in strong wind conditions. In contrast, under gentle wind speeds ($\leqslant$ 3 m

490 s^{-1}), V_R exhibited greater consistency with V_O but there was still a significant down-revision in the

491 average speed in V_R. The average wind speeds of V_O, V_R, and V_T were 2.4, 1.91, and 1.81 m s^{-1},

492 respectively, with V_R exhibiting a 22% decrease compared to V_O. The statistical analysis using the

493 Wilcoxon signed-rank test confirmed a significant difference ($p < 0.01$) in wind speed between V_O and

494 V_T, whereas no significant differences ($p > 0.01$) were found between V_R and V_T. This suggests that

after compensating for UAV motion, attitude, and rotor interference, the wind speed measured by the UAV anemometer is more closely aligned with that measured directly by the meteorological tower. Moreover, under stronger winds, the wind direction values of V_R, V_O, and V_T were relatively similar, yet at weaker winds, V_R showed a small low-bias of about 3.3% (Fig. 9 11 (b)). The mediocre performance of V_R under low wind speeds may originate from the disruption of stable maneuverability in drone rotors caused by low wind speeds, which in turn leads to the failure of the correction algorithm based on CFD steady-state simulations.

Fig. 10 12 presents the wind rose diagrams, offering a detailed overview of the wind speed and direction characteristics for V_R, V_O, and V_T. Compared to the prevailing wind direction frequency (north wind, 39%) of V_T, the dominant wind direction frequency errors for V_O and V_R are 40% and 5% respectively, demonstrating the superiority of V_R in correcting the prevailing wind direction frequency. Meanwhile, deviations in the secondary components introduced by V_R (e.g., northwester wind) indicate directions for subsequent model optimization. Compared to V_O, V_R showed a much improved match between the corrected wind velocity and frequency distributions versus V_T (Fig. 10), both showing predominant northerly winds. In summary, tThese analyses indicated that Eq. 16(23) can effectively correct wind measurement biases induced by UAV disturbances, motion, and attitude changes, particularly at higher wind speeds.

In addition, it should be emphasized that while this study primarily relied on meteorological tower data for algorithm validation, cross-validation through industrial emission scenarios has further confirmed the algorithm's robustness in complex flow fields (Han et al., 2023).

515

516
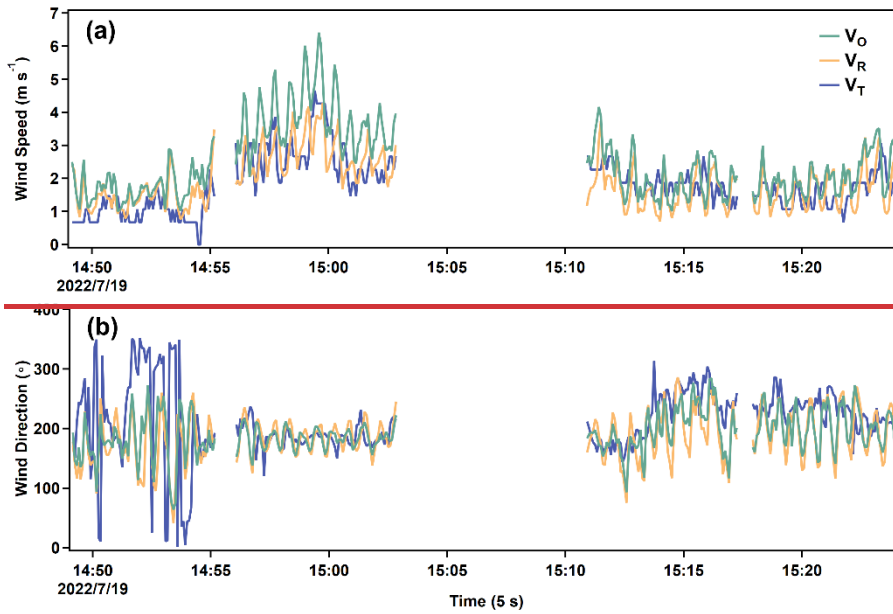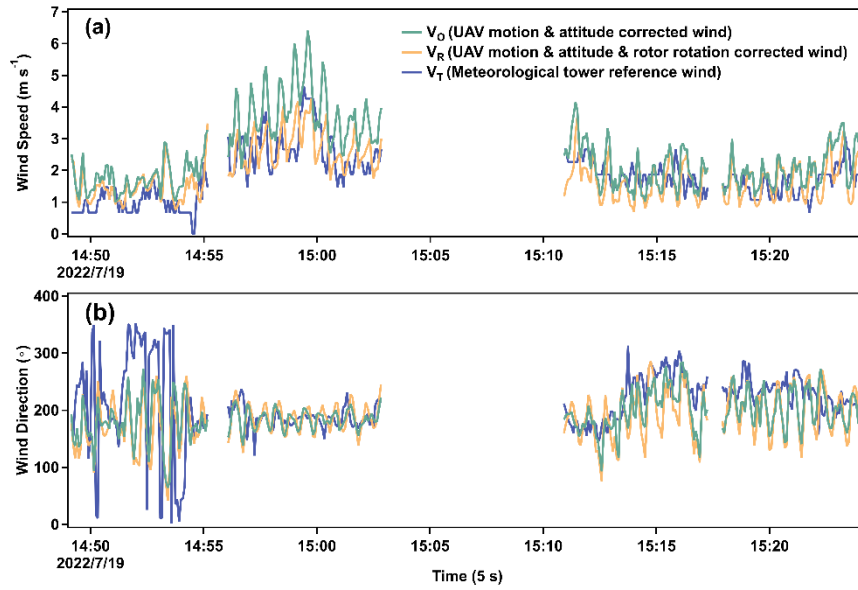
517 **Figure 911: Comparison of wind speed and wind direction time series for V_R, V_O, and V_T. (a) Comparison of**

518 **wind speed time series for V_R, V_O, and V_T. (b) Comparison of wind direction time series for V_R, V_O, and V_T.**

519 **(Note: The meteorological tower measured wind data at 5 s~s~ intervals, while the UAV-based measured and**

520 **corrected wind data were processed with a 10 s sliding average to suppress rotor-induced high-frequency**

521 **noise, followed by 5 s non-overlapping averaging to align temporally with the tower's 5 s output interval.~was~**

522 **~averaged using a 10 s sliding window before calculating 5 s mean values.~)**

523
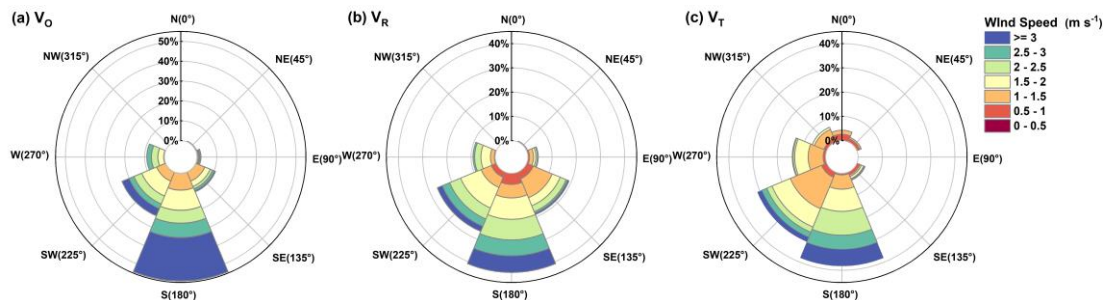
Figure ~~10~~13: Comparison of wind roses for V_O, V_R, ~~V_O,~~ and V_T.

3.6 Discussion on the Limitations of the Algorithm

The current development of algorithms based on idealized steady-state CFD simulations relies on two key assumptions: low environmental turbulence intensity (0.1%) and turbulence length scales dominated by anemometer geometric parameters (0.012 meters). While this idealized setup effectively isolates rotor-induced flow distortion, its turbulence characteristics fundamentally differ from natural atmospheric conditions. However, it is crucial to emphasize that the algorithm's applicability under turbulent conditions remains valid. This is because rotor-induced wind speed deviations exhibit systemic long-time-scale characteristics, whereas atmospheric turbulence primarily affects measurement accuracy through random fluctuations in wind speed and direction with instantaneous nature. This temporal-scale distinction enables our correction algorithm to effectively eliminate systemic biases while minimizing the impact of transient turbulence effects. Nevertheless, it should be noted that under stable atmospheric conditions (low wind speeds) as discussed in Sec. 3.5 or extreme weather scenarios, such airflow environments may disrupt the stable manoeuvrability of UAV rotors or obscure the systemic drainage effects of rotors, potentially leading to a nonlinear degradation in algorithm accuracy.

In addition, another limitation of our study is the assumption of a smooth surface in CFD simulations, which does not fully capture the impact of surface roughness on wind speed variations near the ground. In reality, surface roughness elements (e.g., vegetation, buildings, or terrain irregularities) alter the wind profile, increasing turbulence and wind shear in the atmospheric surface layer. This effect is particularly relevant for UAV-based wind measurements at low altitudes.

To further enhance the correction algorithm's applicability under diverse environmental conditions, future research will focus on the following aspects: conducting sensitivity studies under different turbulence intensity conditions, implementing supplementary correction modules specifically targeting atmospheric turbulence, and incorporating surface roughness length parameters in future CFD simulations. Although atmospheric turbulence presents significant challenges for UAV-based wind measurements, the correction framework established in this study has demonstrated its effectiveness in improving measurement accuracy across diverse meteorological conditions, thereby laying a critical foundation for developing reliable UAV-based wind measurement systems.

4 Conclusions

The scenarios involving direct measurements of wind fields within the atmospheric boundary layer using multirotor UAVs have become progressively commonplace, heightening the significance of accurate wind assessment. However, the rotor propellers during UAV flight introduce additional induced flows at the anemometer location, leading to false wind speed signals. For the present UAV-anemometer-payload configuration, a CFD-based method was used to simulate the process of the UAV wind measurement platform during stable flights under headwind, tailwind, and crosswind conditions. The analyses of induced airflows surrounding the anemometer led to a predictive tool for disturbance airflows. Building upon the UAV motion and attitude correction algorithm, a correction algorithm was proposed for the combined false wind signals from UAV rotor propeller disturbance, motion, and attitude changes during UAV flights. Through comparison of the corrected wind speeds derived from measurements taken from the UAV platform and concurrent three-dimensional wind measurements from a nearby meteorological tower, the validity of the correction algorithm has been demonstrated. Although the algorithm still has certain limitations, it provides a feasible approach for the direct measurement of wind speed from multirotor UAV flights. ~~This result presents a viable approach for directly measuring wind speeds with good accuracy from multirotor UAV flights. Indeed, during the first application of the UAV measurement platform to determine greenhouse gas emission rates from a large coking plant in one of the largest steelmaker in the country, we have demonstrated that the emission rates determined on the basis of greenhouse gas concentration and three-dimensional wind measurements match closely with emission rates determined from material balance (Han T, 2023), again providing a secondary validation of such a correction algorithm.~~

In conclusion, this study represents a significant advancement in three-dimensional wind speed measurement using UAV platforms, presenting a practical and effective method for direct and accurate wind measurement. This technological breakthrough not only creates a strong foundation for precise wind field measurements with UAVs but also provides potential avenues for the accurate quantification of gaseous pollutant emissions based on UAV. The outcomes of this work carry considerable scientific importance and offer valuable practical applications.

Data availability: Data will be made available on request.

Acknowledgment: This project was supported by a grant from the National Natural Science Foundation of China Creative Research Group Fund (22221004).

Declaration of competing interest: The contact author has declared that none of the authors has any competing interests.

Reference

Afaq, M. and Ahmad, R.: Comparison Between ANSYS Fluent and Solidworks Internal Flow Simulation for Analysis of A Fuzzy Logic Controller-Based Heating/Cooling System in A Mobile Robot Design, In: 2023 International Conference on Robotics and Automation in Industry (ICRAI), IEEE, 1-6, 10.1109/ICRAI57502.2023.10089571, 2023.

Anderson, K. and Gaston, K. J.: Lightweight unmanned aerial vehicles will revolutionize spatial ecology, Front. Ecol. Environ., 11, 138-146, https://doi.org/10.1890/120150, 2013.

Azmi, M. F. M., Marzuki, M. A. B., and Bakar, M. A. A.: Vehicle aerodynamics analysis of a multi-purpose vehicle using CFD, ARPN Journal of Engineering and Applied Sciences, 12, 2345-2350, 2017.

Barbieri, L., Kral, S. T., Bailey, S. C. C., Frazier, A. E., Jacob, J. D., Reuder, J., Brus, D., Chilson, P. B., Crick, C., Detweiler, C., Doddi, A., Elston, J., Foroutan, H., Gonzalez-Rocha, J., Greene, B. R., Guzman, M. I., Houston, A. L., Islam, A., Kemppinen, O., Lawrence, D., Pillar-Little, E. A., Ross, S. D., Sama, M. P., Schmale, D. G., Schuyler, T. J., Shankar, A., Smith, S. W., Waugh, S., Dixon, C., Borenstein, S., and de Boer, G.: Intercomparison of small unmanned aircraft system (sUAS) measurements for atmospheric science during the LAPSE-RATE campaign, Sensors (Basel), 19, https://doi.org/10.3390/s19092179, 2019.

Bonin, T. A., Chilson, P. B., Zielke, B. S., Klein, P. M., and Leeman, J. R.: Comparison and application of wind retrieval algorithms for small unmanned aerial systems, Geosci. Instrum., Methods Data Syst., 2, 177-187, https://doi.org/10.5194/gi-2-177-2013, 2013.

Booij, N., Ris, R. C., and Holthuijsen, L. H.: A third-generation wave model for coastal regions: 1. Model description and validation, J. Geophys. Res.: Oceans, 104, 7649-7666, https://doi.org/10.1029/98JC02622, 1999.

Crowe, D., Pamula, R., Cheung, H. Y., and De Wekker, S. F.: Two supervised machine learning approaches for wind velocity estimation using multi-rotor copter attitude measurements, Sensors, 20,

5638, https://doi.org/10.3390/s20195638, 2020.

de Divitiis, N.: Wind estimation on a lightweight vertical-takeoff- and-landing uninhabited vehicle, J. Aircr., 40, 759-767, https://doi.org/10.2514/2.3155, 2003.

Dao, M. H., Zhang, B., Xing, X., Lou, J., Tan, W. S., Cui, Y., and Khoo, B. C.: Wind tunnel and CFD studies of wind loadings on topsides of offshore structures, Ocean Eng., 285, 115310, https://doi.org/10.1016/j.oceaneng.2023.115310, 2023.

Donnell, G. W., Feight, J. A., Lannan, N., and Jacob, J. D.: Wind characterization using onboard IMU of sUAS, In: 2018 Atmospheric flight mechanics conference, 2986, https://doi.org/10.2514/6.2018-2986, 2018.

Drob, D. P., Emmert, J. T., Meriwether, J. W., Makela, J. J., Doornbos, E., Conde, M., Hernandez, G., Noto, J., Zawdie, K. A., McDonald, S. E., Huba, J. D., and Klenzing, J. H.: An update to the Horizontal Wind Model (HWM): The quiet time thermosphere, Earth Space Sci., 2, 301-319, https://doi.org/10.1002/2014EA000089, 2015.

Elston, J., Argrow, B., Stachura, M., Weibel, D., Lawrence, D., and Pope, D.: Overview of small fixed-wing unmanned aircraft for meteorological sampling, J. Atmos. Ocean. Technol., 32, 97-115, https://doi.org/10.1175/Jtech-D-13-00236.1, 2015.

Gonzalez-Rocha, J., Woolsey, C. A., Sultan, C., and De Wekker, S. F. J.: Sensing wind from quadrotor motion, J. Guid. Control Dyn., 42, 836-852, https://doi.org/10.2514/1.G003542, 2019.

Gousseau, P., Blocken, B., Stathopoulos, T., and van Heijst, G. J. F.: CFD simulation of near-field pollutant dispersion on a high-resolution grid: A case study by LES and RANS for a building group in downtown Montreal, Atmos. Environ., 45, 428-438, https://doi.org/10.1016/j.atmosenv.2010.09.065, 2011.

Gryning, S. E., Holtslag, A. A. M., Irwin, J. S., and Sivertsen, B.: Applied dispersion modelling based on meteorological scaling parameters, Atmos. Environ., 21, 79-89, https://doi.org/10.1016/0004-6981(87)90273-3, 1987.

Haleem, A.: Vehicular Aerodynamics Wind Tunnel Testing of Unmanned Aerial Multirotor Vehicles and Wall Interference Corrections, PhD Thesis, Toronto Metropolitan University, 2021.

Han T, X. C., Liu Y, Yang Y, Zhang Y, Huang Y, Gao X, Zhang X., Bao F, and Li S-M.: Application of a new UAV measurement methodology to the quantification of CO_2 and CH_4 emissions from a major

coking plant, Atmos. Meas. Tech., 1-21, https://doi.org/10.5194/amt-17-677-2024, 2023.

Hedworth, H., Page, J., Sohl, J., and Saad, T.: Investigating Errors Observed during UAV-Based Vertical Measurements Using Computational Fluid Dynamics, Drones, 6, 253, https://doi.org/10.3390/drones6090253, 2022.

Hoang, M. L., Carratu, M., Paciello, V., and Pietrosanto, A.: Noise Attenuation on IMU Measurement For Drone Balance by Sensor Fusion, in: 2021 IEEE International Instrumentation and Measurement Technology Conference (I2MTC), 1-6, https://doi.org/10.1109/i2mtc50364.2021.9460041, 2021.

Johansen, T. A., Cristofaro, A., Sorensen, K., Hansen, J. M., and Fossen, T. I.: On estimation of wind velocity, angle-of-attack and sideslip angle of small UAVs using standard sensors, in: 2015 International Conference on Unmanned Aircraft Systems (ICUAS), 510-519, https://doi.org/10.1109/icuas.2015.7152330, 2015.

Jonuskaite, A.: Flow simulation with SolidWorks, 2017.

Kim, M.-S. and Kwon, B. H.: Estimation of sensible heat flux and atmospheric boundary layer height using an unmanned aerial vehicle, Atmosphere, 10, 363, https://doi.org/10.3390/atmos10070363, 2019.

Langelaan, J. W., Alley, N., and Neidhoefer, J.: Wind field estimation for small unmanned aerial vehicles, J. Guid. Control Dyn., 34, 1016-1030, https://doi.org/10.2514/1.52532, 2011.

Martin, S., Bange, J., and Beyrich, F.: Meteorological profiling of the lower troposphere using the research UAV "M^{2}AV Carolo", Atmos. Meas. Tech., 4, 705-716, https://doi.org/10.5194/amt-4-705-2011, 2011.

McGonigle, A., Aiuppa, A., Giudice, G., Tamburello, G., Hodson, A., and Gurrieri, S.: Unmanned aerial vehicle measurements of volcanic carbon dioxide fluxes, Geophys. Res. Lett., 35, https://doi.org/10.1029/2007GL032508, 2008.

Neumann, P. P. and Bartholmai, M.: Real-time wind estimation on a micro unmanned aerial vehicle using its inertial measurement unit, Sens. Actuators, A, 235, 300-310, https://doi.org/10.1016/j.sna.2015.09.036, 2015.

Niedzielski, T., Skjøth, C., Werner, M., Spallek, W., Witek, M., Sawiński, T., Drzeniecka-Osiadacz, A., Korzystka-Muskała, M., Muskała, P., and Modzel, P.: Are estimates of wind characteristics based on measurements with Pitot tubes and GNSS receivers mounted on consumer-grade unmanned aerial vehicles applicable in meteorological studies?, Environ. Monit. Assess., 189, 1-18,

https://doi.org/10.1007/s10661-017-6141-x, 2017.

Nolan, P. J., Pinto, J., Gonzalez-Rocha, J., Jensen, A., Vezzi, C. N., Bailey, S. C. C., de Boer, G., Diehl, C., Laurence, R., Powers, C. W., Foroutan, H., Ross, S. D., and Schmale, D. G.: Coordinated unmanned aircraft system (UAS) and ground-based weather measurements to predict Lagrangian coherent structures (LCSs), Sensors (Basel), 18, https://doi.org/10.3390/s18124448, 2018.

Oktay, T. and Eraslan, Y.: Computational fluid dynamics (Cfd) investigation of a quadrotor UAV propeller, International Conference on Energy, Environment and Storage of Energy, 21-25,

Palomaki, R. T., Rose, N. T., van den Bossche, M., Sherman, T. J., and De Wekker, S. F.: Wind estimation in the lower atmosphere using multirotor aircraft, J. Atmos. Ocean. Technol., 34, 1183-1191, https://doi.org/10.1175/JTECH-D-16-0177.1, 2017.

Pettersson, K. and Rizzi, A.: Aerodynamic scaling to free flight conditions: Past and present, Prog. Aerosp. Sci., 44, 295-313, https://doi.org/10.1016/j.paerosci.2008.03.002, 2008.

Quan, Q.: Introduction to Multicopter Design and Control, Springer Singapore, 384 pp., https://doi.org/10.1007/978-981-10-3382-7, 2017.

Ramya, P., Kumar, A. H., Moturi, J., and Ramanaiah, N.: Analysis of flow over passenger cars using computational fluid dynamics, Int J Eng Trends Technol (IJETT), 29, 170-176, 10.14445/22315381/IJETT-V29P232 2015.

Rautenberg, A., Graf, M. S., Wildmann, N., Platis, A., and Bange, J.: Reviewing wind measurement approaches for fixed-wing unmanned aircraft, Atmosphere, 9, https://doi.org/10.3390/atmos9110422, 2018.

Riddell, K. D. A.: Design, testing and demonstration of a small unmanned aircraft system (SUAS) and payload for measuring wind speed and particulate matter in the atmospheric boundary layer, University of Lethbridge, Canada, 2014.

Rogers, K. and Finn, A.: Three-dimensional UAV-based atmospheric tomography, J. Atmos. Ocean. Technol., 30, 336-344, https://doi.org/10.1175/JTECH-D-12-00036.1, 2013.

Seibert, P., Beyrich, F., Gryning, S. E., Joffre, S., Rasmussen, A., and Tercier, P.: Review and intercomparison of operational methods for the determination of the mixing height, Atmos. Environ., 34, 1001-1027, https://doi.org/10.1016/S1352-2310(99)00349-0, 2000.

Shaw, J. T., Shah, A. D., Yong, H., and Allen, G.: Methods for quantifying methane emissions using

unmanned aerial vehicles: a review, Philos. T. Roy. Soc. A, 379, https://doi.org/10.1098/rsta.2020.0450, 2021.

Shimura, T., Inoue, M., Tsujimoto, H., Sasaki, K., and Iguchi, M.: Estimation of wind vector profile using a hexarotor unmanned aerial vehicle and its application to meteorological observation up to 1000 m above surface, J. Atmos. Ocean. Technol., 35, 1621-1631, https://doi.org/10.1175/JTECH-D-17-0186.1, 2018.

Sikkel, L., de Croon, G., De Wagter, C., and Chu, Q.: A novel online model-based wind estimation approach for quadrotor micro air vehicles using low cost MEMS IMUs, In: 2016 IEEE/RSJ International Conference on Intelligent Robots and Systems (IROS), IEEE, 2141-2146, 10.1109/IROS.2016.7759336, 2016.

Simma, M., Mjøen, H., and Boström, T.: Measuring wind speed using the internal stabilization system of a quadrotor drone, Drones, 4, 23, https://doi.org/10.3390/drones4020023, 2020.

Soddell, J. R., McGuffie, K., and Holland, G. J.: Intercomparison of atmospheric soundings from the Aerosonde and radiosonde, J. Appl. Meteorol., 43, 1260-1269, https://doi.org/10.1175/1520-0450(2004)043<1260:IOASFT>2.0.CO;2, 2004.

Spiess, T., Bange, J., Buschmann, M., and Vorsmann, P.: First application of the meteorological Mini-UAV 'M^{2}AV', Meteorol. Z., 16, 159-170, https://doi.org/10.1127/0941-2948/2007/0195, 2007.

Stewart, M., Martin, S., and Barrera, N., Barrera, N. (Ed.): Unmanned aerial vehicles: fundamentals, components, mechanics, and regulations, Unmanned Aerial Vehicles, Nova Science Publishers, Hauppauge, New York, USA, 71 pp.2021.

Stockie, J. M.: The mathematics of atmospheric dispersion modeling, SIAM Rev., 53, 349-372, https://doi.org/10.1137/10080991X, 2011.

Thielicke, W., Hubert, W., Muller, U., Eggert, M., and Wilhelm, P.: Towards accurate and practical drone-based wind measurements with an ultrasonic anemometer, Atmos. Meas. Tech., 14, 1303-1318, https://doi.org/10.5194/amt-14-1303-2021, 2021.

van Hooff, T. and Blocken, B.: Coupled urban wind flow and indoor natural ventilation modelling on a high-resolution grid: A case study for the Amsterdam ArenA stadium, Environ. Model. Softw., 25, 51-65, https://doi.org/10.1016/j.envsoft.2009.07.008, 2010.

Vardoulakis, S., Fisher, B. E. A., Pericleous, K., and Gonzalez-Flesca, N.: Modelling air quality in street

725   canyons: a review, Atmos. Environ., 37, 155-182, https://doi.org/10.1016/S1352-2310(02)00857-9,

726   2003.

727   Villa, T. F., Gonzalez, F., Miljievic, B., Ristovski, Z. D., and Morawska, L.: An overview of small

728   unmanned aerial vehicles for air quality measurements: Present applications and future prospectives,

729   Sensors (Basel), 16, https://doi.org/10.3390/s16071072, 2016.

730   Yang, Y., Zhou, J., Xie, C., Tian, W., Xue, M., Han, T., Chen, K., Zhang, Y., Liu, Y., and Huang, Y.: A

731   New Methodology for High Spatiotemporal Resolution Measurements of Air Volatile Organic

732   Compounds: From Sampling to Data Deconvolution, Environ. Sci. Technol., 58, 12488-12497, 2024.

733